TUDelft

Delft University of Technology

Modeling of Resonant Tunneling Diode Oscillators Based on the Time-Domain Boundary Element Method

Lasisi, S.O.; Benson, T.M. ; Greenaway, M.T. ; Gradoni, G. ; Cools, K.

Citation (APA)
Lasisi, S. O., Benson, T. M., Greenaway, M. T., Gradoni, G., & Cools, K. (2022). Modeling of Resonant Tunneling Diode Oscillators Based on the Time-Domain Boundary Element Method. *IEEE Journal on Multiscale and Multiphysics Computational Techniques*, *7*, 161-167. Article 9809810. https://doi.org/10.1109/JMMCT.2022.3187022

Important note
To cite this publication, please use the final published version (if applicable).
Please check the document version above.

Modeling of Resonant Tunneling Diode Oscillators Based on the Time-Domain Boundary Element Method

Shakirudeen O. Lasisi [ID], Trevor M. Benson [ID], Mark T. Greenaway [ID], Gabriele Gradoni [ID], *Member, IEEE*, and Kristof Cools

Abstract—We demonstrate how the coupling of a full-wave time-domain boundary element method (BEM) solver with a circuit solver can be used to model 1) the generation of high frequency oscillations in resonant tunneling diode (RTD) oscillators, and 2) the mutual coupling and synchronization of non-identical RTDs with significant differences in frequencies to achieve coherent power combination. Numerical simulations show a combined output power of up to 3.7 times a single oscillator in synchronized devices. The non-differential conductance of the RTD is modeled as a lumped component with a non-linear current-voltage relationship. The lumped element is coupled to the radiating structure using a finite-gap model in a consistent and discretisation independent manner. The resulting circuit equations are solved simultaneously and consistently with time-domain electric field integral equations that model the transient scattering of electromagnetic (EM) fields from conducting surfaces that make up the device. This paper introduces three novel elements: (i) the application of a mesh independent feed line to the modelling of feed lines of RTD devices, (ii) the coupling of the radiating system to a strongly non-linear component with negative differential resistance, and (iii) the verification of this model with circuit models where applicable and against the experimental observation of synchronisation when two RTDs are placed in close proximity. These three elements provide a methodology that create the capacity to model RTD sources and related technology.

Index Terms—BEM, TD-BEM, modeling, RTD, terahertz, THz, oscillators.

I. INTRODUCTION

THE design and modeling of oscillators and switching devices that operate in the terahertz (THz) spectrum is an area of active research with many promising applications [1]. Resonant tunneling diode (RTD) oscillators where a strongly non-linear I-V characteristic with negative differential conductance arises from quantum mechanical tunnelling between two contacts [2] are shown to achieve the highest frequencies among the family of solid state electronic sources of terahertz oscillations (e.g. Gunn, TUNETT and IMPATT diodes) [3]. However, their output power, of the order of micro-Watts (μW), limits their applicability. To achieve higher output power, multiple devices could be coupled together in an array arrangement with all elements oscillating in synchronism with the same frequency.

Earlier studies of microwave and terahertz generation in synchronized devices have mostly focused on experimental observations and theoretical formulations using equivalent circuit representations to analyze and characterize the devices [3], [4]. Whereas physical characterization takes time and resources, circuit simulations are not sufficiently accurate to describe the effect of the device's environment. Full-wave electromagnetic simulations provide the best alternative for such applications. Solutions constructed via BEMs automatically and perfectly fulfil the radiation condition away from the device, removing the need to implement approximate boundary conditions such as the perfectly matched layer [5] as often encountered in finite element methods or finite difference time domain approaches. In addition, the BEM utilizes surface meshing as compared to discretizing the volume of the radiating structure, resulting in algorithms that are more economic, both in their time and memory usage. The time-domain formulation permits simulation over a range of frequencies and allows observation of both transient and steady state responses. The RTD device is strongly non-linear, leaving only time domain methods as viable tools for modelling. Frequency sweeps followed by inverse Fourier transforms are not an option for this application. The primary unknown is the surface current density. Secondary quantities of interest, such as the near field, radiation efficiency, port impedance, etc. can be computed easily in a post-processing step.

The integration of circuit and full wave time-domain field solvers to account for lumped circuit impedances in electromagnetic simulations have been explored by several authors. More recent are developments in the integration of circuit simulators with time-domain integral equation (TDIE) solvers. These methods are useful for the simultaneous solution of
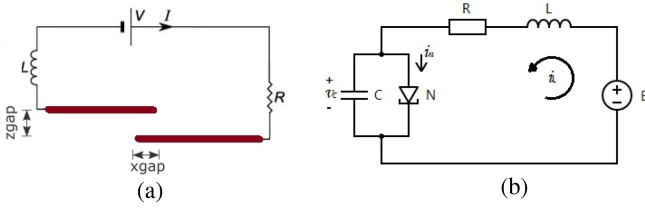
Fig. 1. (a) Approximate model of an RTD Oscillator showing two overlapping conductive plates (burgundy online) separated by a tunnel barrier in a resonant circuit. Current flows/tunnels between the top and bottom plates. (b) Simple circuit representation of the oscillator where 'N' is the non-linear lumped component representing the I-V characteristic across the tunnel gap of the RTD.

active and nonlinear microwave circuits along with connected 2D/3D structures while keeping the benefits of integral equation formulations. So far they have been applied to the analysis of shielded amplifiers [6] and loaded patch antennas [7] in the microwave regime.

This paper presents a modelling methodology that for the first time takes into account, in a mutually coupled and fully integrated fashion, the dynamics of both the RTD and the radiating structure in which it is embedded. In this paper, a full wave time-domain integral equation solver using a classical marching-on-in-time (MOT) algorithm is used to model the generation of sub-terahertz oscillations and mutual coupling in RTD devices that exhibit non-differential conductance (NDC) (see Fig. 1). The paper introduces three main novel elements in the modelling of this class of devices. First, the non-linear current-voltage (I-V) characteristic presented by the tunnel barrier of the device is treated as a discrete two port non-linear component connected with the device. While connected components are considered lumped, the ports are finite in size and at a finite distance apart. By carefully interfacing field and circuit solvers, the resulting coupled system of non-linear equations is solved by marching-on-in-time. This is the first demonstration of the coupling of a TD-BEM method with a circuit that exhibits a region of negative differential resistance. This approach takes into account the mutual coupling of the radiating system and the non-linear circuit and the capacitive and inductive behaviour of the radiating structure. In existing models, capacitive and inductive effects are included by fine-tuning the circuit parameters of the model, rather than by ab initio simulation. Second, our approach incorporates the mesh independent port modelling developed in [8] for both the feed lines and the connection of the RTD to the radiating structure. Finally, this paper verifies the correctness in those regions where other solution methods are available by comparing the working frequency with that of a tuned circuit model. We also verify that the experimentally observed phenomenon of frequency locking is correctly predicted by our modelling paradigm.

Parameters such as the far field and radiating power are calculated to observe the radiation pattern away from the device and the relative output power of a single RTD oscillator to a coupled device. This approach enables the design of an array of oscillators operating at a given frequency with output power suitable for wireless data transmission, portable scanners and handheld imaging devices.

II. FORMULATION

Consider a simplified representation of a resonant tunneling diode oscillator [9] modeled by the surface $\Gamma = \Gamma_1 \cup \Gamma_0$ comprising two slightly overlapping metal plates (Fig. 1(a)). Due to the highly conductive nature of the materials that typically make up the device layers, the plates are treated as perfect electric conductors (PEC). Current is allowed to tunnel between the overlapping regions of both plates. The actual solid state physics governing the tunneling process is unique to the specific type of RTD device and details can be found in several other papers [9]–[12]. For simplicity, the tunnel barrier (material between the conductive plates) is taken to have the same properties as the surrounding medium (vacuum). The diode exhibits negative differential conductance (NDC) in its strongly non-linear I-V characteristic between the plates. When biased in the NDC region, the device is able to generate self-sustained oscillations in the presence of a resonant circuit [13]. The exact frequency and amplitude of the oscillations depends not only on the RTD but also on the radiating structure. As such, an integrated simulation methodology is required.

Consider a simple configuration comprising the RTD connected to the terminals of a battery. The intrinsic junction capacitance and the inductance present in the plates give rise to C and L. This circuit, as shown in Fig. 1, may be modified to include additional sources of inductance, capacitance and resistance in the form of e.g a ground plane, cavity or lumped circuit components. These sources of impedance may also include finite battery resistance, lead inductance etc. present in a practical circuit. To capture the interactions between electromagnetic fields and the device materials, we begin the formulation by considering the transient scattering problem. Given an incident electric field $e^i(r, t)$, the scattered field can be computed from the induced current on the plates through the application of the single layer time domain operator:

$$\hat{n} \times p.v. \int_\Gamma \text{grad} \frac{\text{div}\, j(r', t-\tau)}{4\pi\epsilon_0 R} ds'$$

$$- \hat{n} \times \mu_0 \int_\Gamma \frac{\partial_t^2 j(r', t-\tau)}{4\pi R} ds'$$

$$= -\hat{n} \times \partial_t e^i(r, t) \tag{1}$$

where $R = |r - r'|$, and $\tau = \frac{R}{c_0}$. The current is approximated by a linear expansion,

$$j(r', t) \cong \sum_{m=1}^{N_s} \sum_{l=1}^{N_t} a_m^l f_m(r') T(t - l\Delta t) \tag{2}$$

where f_m are the enriched Rao-Wilton-Glisson or RWG spatial basis described in [8] excluding the 'varying' half-RWGs, T are 3 rd degree shifted piece-wise polynomial Lagrange interpolators, and a_m^l are the unknown weighting coefficients. The choice of basis functions corresponds to a current injection/extraction that is uniformly distributed along the port of the device. This is a good approximation of the physical behaviour and improved upon injection at a single mesh node. Other finite-gap lumped-port models have been recently proposed [14], [15].

In the BEM, current in (1) is discretized using (2), tested using a Galerkin scheme in space and collocated in time. This yields a system of equations which can be written in matrix form as:

$$Z^0 I^k = -E^{i,k} - \sum_{l=1}^{k-1} Z^{(k-l)} I^l \qquad (3)$$

where the matrix Z, and vector E^i are given by:

$$Z_{nm}^{(k-l)} = -\eta \int_\Gamma \operatorname{div} \boldsymbol{f}_n(\boldsymbol{r}) \int_\Gamma c_0 \frac{\operatorname{div} \boldsymbol{f}_m(\boldsymbol{r}') T^{(k-l)}}{4\pi R} ds' ds$$
$$-\eta \int_\Gamma \boldsymbol{f}_n(\boldsymbol{r}) \int_\Gamma \frac{\boldsymbol{f}_m(\boldsymbol{r}') \partial_t^2 T^{(k-l)} dt}{4\pi c_0 R} ds' ds \qquad (4)$$

$$E_n^{i,k} = \int_\Gamma \boldsymbol{f}_n(r) \cdot \partial_t \boldsymbol{e}^i(\boldsymbol{r}, k\Delta t) ds \qquad (5)$$

and where $\eta = \sqrt{\mu_0/\epsilon_0}$, $I^k = [a_1^k, a_2^k \ldots a_{N_s}^k]$, and $T^{(k-l)} = T(k\Delta t - l\Delta t - \tau)$ at $t = k\Delta t$. The above equation is solved at every time step for the unknown current coefficients using the marching-on-in-time algorithm. In [8] it was shown that adding a lumped component or source introduces an additional voltage term, in this case time-dependent, on the left hand side of (3). This correspond to an impressed voltage at the port along the edge where the component is connected. Assuming no incident field, this introduces 4 voltage terms into the equation, corresponding to each lumped component, the source feed and non-linear device. Thus (3) becomes:

$$Z^0 I^k + V_N^k + V_R^k + V_L^k = -V_0^k - \sum_{l=1}^{k-1} Z^{(k-l)} I^l \qquad (6)$$

where

$$V_{x,n}^k = \partial_t v_x^k \int_\gamma \hat{\boldsymbol{m}} \cdot \boldsymbol{f}_n(\boldsymbol{r}) dl = \begin{cases} \partial_t v_x^k, & n \in (\Gamma \cap \gamma) \\ 0 & elsewhere, \end{cases} \qquad (7)$$

the subscript 'x' stands for any of $R, L, N, 0$, and v_x^k are the instantaneous voltages at time $t = k\Delta t$. γ is that part of the boundary of Γ that corresponds to the port at which the lumped element is connected and $\hat{\boldsymbol{m}}$ is the unit vector tangential to Γ and normal to γ.

To solve (6) we need extra equations that relate the voltage terms with the current through their respective components. For a simple 2-port device, this is equal to the current flowing across the edge node where the device is connected i.e. the current coefficient i_x^k at the loading point at any given time $t = k\Delta t$. For the system given in Fig. 1(b), the following set of equations apply:

$$i_N^k = f(v_N^k) \qquad (8)$$

$$i_R^k = \frac{v_R^k}{R} \qquad (9)$$

$$\partial_t i_L^k = \frac{v_L^k}{L} \qquad (10)$$

where $f(v)$ is the non-linear I-V characteristic of the RTD. Circuit techniques such as modified nodal analysis can be used to write out equations for systems with complex circuitry. Equations (6) - (10) together give a coupled set of equations of the order of the degree of freedom of the device.

A. Reduced Algorithm

Solving the system of equations above require solving for N unknowns where $N = number\ of\ internal\ edges + no\ of\ ports + number\ of\ lumped\ components$. This number can easily become very large depending on the size of the mesh. This can cause iterative non-linear solvers to find it difficult to discover a unique solution after several iterations and fail to converge. Here we report a method to reduce the unknowns that are immediately solved for by the non-linear solver to the current at the ports and the voltage over the RTD. The internal currents and voltages over the linear lumped components can then be calculated using appropriate substitutions. This method introduces internal marching-on-in-time operations, and thus more calculation, but can lead to significant increase in the speed of convergence of the non-linear solver per time-step and thus an overall faster solution. This can be attributed to less time spent in long iterations that arise due to poor convergence of the solution at certain time steps of the original system of equations.

We can write eqn (6) as:

$$Z * I + V_N^k + V_R^k + V_L^k = -V_0^k \qquad (11)$$

where

$$Z = \begin{bmatrix} Z_{ii} & Z_{i1} & Z_{i2} \\ Z_{1i} & Z_{11} & Z_{12} \\ Z_{2i} & Z_{21} & Z_{22} \end{bmatrix}, \quad I = \begin{bmatrix} I_{ii} \\ I_1 \\ I_2 \end{bmatrix} \qquad (12)$$

where subscripts $i, 1, 2$ indicate elements of Z and I that live on the internal edges, port 1 and port 2 of Γ. From fig. 1, R, L and V_0 are connected to port 1 (pair of ports connected to the outer edges of the conductive plates) and the non-linear lumped component N representing the non-linear I-V connected to port 2 (pair of ports connected to the inner edges of the conductive plates). It is therefore clear that $i_R = i_L = I_1$ and $i_N = I_2$. From eqn (12) and (7), we can expand eqn (11) as:

$$Z_{ii} * I_{ii} + Z_{i1} * I_1 + Z_{i2} * I_2 = 0 \qquad (13)$$

$$Z_{1i} * I_{ii} + Z_{11} * I_1 + Z_{12} * I_2 + \partial_t v_R^k + \partial_t v_L^k = -\partial_t v_0^k \qquad (14)$$

$$Z_{2i} * I_{ii} + Z_{21} * I_1 + Z_{22} * I_2 + \partial_t v_N^k = 0 \qquad (15)$$

We can expand (13) and write the internal currents I_{ii}^k at the present time-step in terms of previous current values and present currents at the ports:

$$I_{ii}^k = (Z_{ii}^0)^{-1} \left(-Z_{i1}^0 I_1^k - Z_{i2}^0 I_2^k - \sum_{l=1}^{k-1} Z_i^{(k-l)} I^l \right) \qquad (16)$$

where $Z_x = [Z_{xi} \ Z_{x1} \ Z_{x2}]$ and $x \in \{i, 1, 2\}$. Equation (16) can be solved at every time step using marching-on-in-time. We

substitute (9), (10) and (16) in (14) and (15):

$$Z_{1i}^0\left[(Z_{ii}^0)^{-1}\left(-Z_{i1}^0I_1^k - Z_{i2}^0I_2^k - \sum_{l=1}^{k-1}Z_i^{(k-l)}I^l\right)\right]$$
$$+ Z_{11}^0I_1^k + Z_{12}^0I_2^k + R\partial_tI_1^k + L\partial_t^2I_1^k$$
$$= -\partial_tv_0^k - \sum_{l=1}^{k-1}Z_1^{(k-l)}I^l \tag{17}$$

$$Z_{2i}^0\left[(Z_{ii}^0)^{-1}\left(-Z_{i1}^0I_1^k - Z_{i2}^0I_2^k - \sum_{l=1}^{k-1}Z_i^{(k-l)}I^l\right)\right]$$
$$+ Z_{21}^0I_1^k + Z_{22}^0I_2^k + \partial_tv_N^k = -\sum_{l=1}^{k-1}Z_2^{(k-l)}I^l \tag{18}$$

(8), (17) and (18) forms a new set of equation with 3 unknowns I_1, I_2 and V_N which can be solved using MOT at every time step. The internal currents can be calculated accordingly using eqn (16)

B. Circuit Model

For verification purposes, a simple circuit model is presented. In the high frequency regime and for a low-order circuit, it is not expected that the results of both methods will match. However, the results should be within the neighborhood of each-other and useful enough for verification purposes. Fig. 1(b) shows the equivalent circuit representation for the system in Fig. 1(a). L is the equivalent sum of the geometric and lumped inductances, and C is the geometric capacitance which is dominated by the junction capacitance between the two plates. The impedances are computed from the full-wave BEM method. The state variables v_c and i_L representing the voltage across the capacitor and the current through the inductor can be calculated by solving the system of equations:

$$v_c' = \frac{1}{C}\left(-i_n(v_c) + i_L\right) \tag{19}$$

$$i_L' = \frac{1}{L}\left(E - Ri_L - v_c\right) \tag{20}$$

The output frequency is largely dependent on L, C, the negative differential resistance of the static I-V curve at the bias point R_n and positive resistance R, and can be estimated as [9], [13]:

$$f_{exp} = \alpha \times \omega_N \tag{21}$$

where ω_N is the natural frequency,

$$\alpha = \sqrt{\left(1 - \frac{R}{R_n}\right) - \frac{(1 - Q^2R/R_n)^2}{4Q^2}} \tag{22}$$

and the quality factor is given by $Q = R_n\sqrt{C/L}$. The system will therefore oscillate only when the term inside the square root in (22) evaluates to a positive value and when $(R_n/R - Q^2)$ > 0.
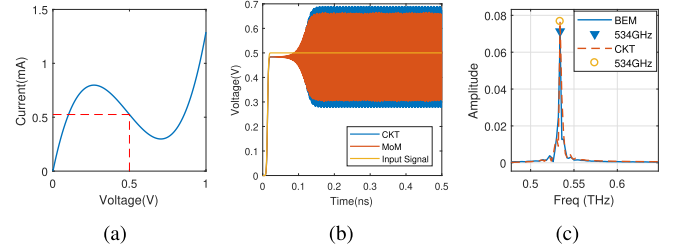

Fig. 2. (a) The I-V characteristic of the RTD with the bias point shown in dashed lines (b) Self-sustained voltage oscillations at the output port (across the tunnel gap). (c) The spectrum of the voltage oscillations.

C. Circuit Model: Coupled Oscillators

In the case of multiple closely spaced oscillators, we assume that inductive/magnetic coupling is the principal mechanism for coupling between the devices. Hence, similar to transformer circuits, a mutual inductance value $M_{12} = M_{21} = M$ is calculated and incorporated into the circuit equations to account for the mutual coupling between the oscillators. The state equations can thus be written as:

$$v_{c_1}' = \frac{1}{C_1}\left(-i_{n_1}(v_{c_1}) + i_{L_1}\right) \tag{23}$$

$$i_{L_1}' = \frac{1}{L_1}\left(E_1 - R_1i_{L_1} - v_{c_1} - Mi_{L_2}'\right) \tag{24}$$

$$v_{c_2}' = \frac{1}{C_2}\left(-i_{n_2}(v_{c_2}) + i_{L_2}\right) \tag{25}$$

$$i_{L_2}' = \frac{1}{L_2}\left(E_2 - R_2i_{L_2} - v_{c_2} - Mi_{L_1}'\right) \tag{26}$$

III. Examples

A. Model of a Single Oscillator

Fig. 1 shows the structure of the considered device. The dimensions of the top and bottom plates are $25\,\mu m \times 25\,\mu m$ with an overlapping area of $5\,\mu m \times 25\,\mu m$ separated by a vertical distance of $1\,\mu m$. The geometric inductance of the device is estimated to be approximately $L = \frac{V_L}{j\omega I_L} = 11.26$ pH and the capacitance $C = \frac{I_C}{j\omega V_C} = 0.002$ pF using a frequency-domain BEM at the fundamental frequency of oscillation.

The static voltage controlled I-V characteristic for the RTD is approximated using a cubic polynomial function

$$I(v) = 0.01 * (1.2v^3 - 1.752v^2 + 0.681v)$$

constructed to resemble N-type I-V curves commonly found in RTDs as shown in Fig. 2(a). The device is biased around the midpoint of the NDR region of the I-V curve. At the point of bias $Rn = \Delta V/\Delta I = -595\,\Omega$. A positive resistor of $R = 0.05\,Rn = 29.8\,\Omega$, and lumped inductance of $L = 25$ pH is added as in the configuration of Fig. 1. The input voltage is given by

$$V_0(t) = A * (erf.(t/w - dx) + a)$$

where $A = V_{dc}/2$, $w = 20\Delta t$, $dx = 4$, $a = erf(4)$, and represents a voltage that is gradually turned on until it stabilizes
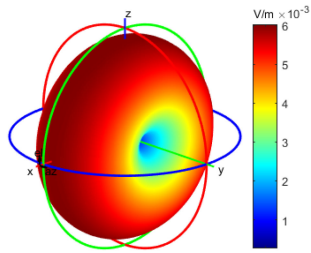
Fig. 3. 3D far-field plot of a single RTD oscillator at the fundamental frequency $f = 534$ GHz computed using the TD-BEM method.
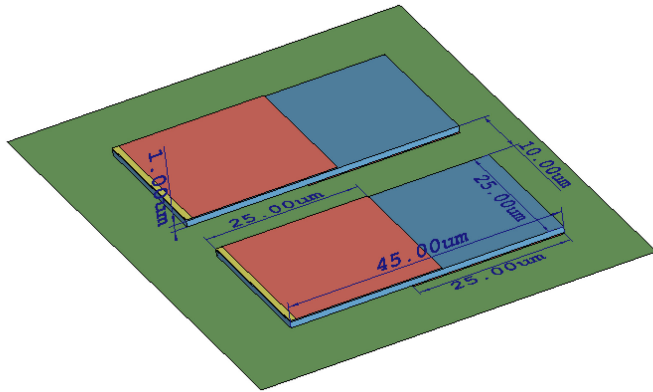

Fig. 4. 3D Model of two RTD oscillators placed side-by-side within the near-field of each-other with an underlying metallic ground plane (green online). Top conductive plate shown in burgundy (online) and barrier between plates shown in blue.
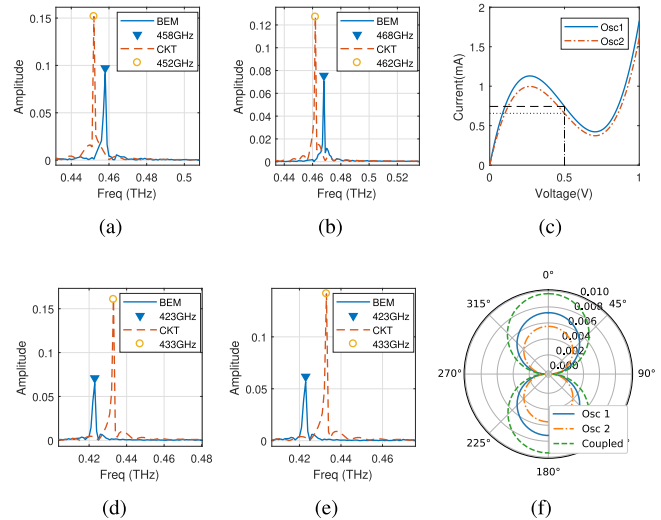

Fig. 5. (a) The spectra of Oscillator 1 in the absence of Oscillator 2. (b) The spectra of Oscillator 2 in the absence of Oscillator 1. (c) The I-V relationship of the RTDs for both oscillators with the bias points shown in dashed lines. (d) The spectra of Oscillator 1 when both oscillators are placed side by side. (e) The spectra of Oscillator 2 when both oscillators are placed side by side. (f) The E-Theta radiation pattern (Phi Sweep) in the far-field at $\theta = \pi/2$ in V/m.
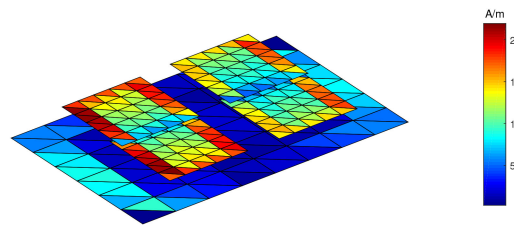

Fig. 6. Face currents at the fundamental frequency $f = 423$ GHz.

at the desired DC bias voltage. The terms dx, and a shift and raise the function so that $V_0(0) = 0$. A is the amplitude and w determines the width or time it takes the signal to reach its DC value from zero. The results presented in Fig. 2 show the output voltage wave-forms and spectrum from TD-BEM and circuit (CKT) simulations. Both sets of results show fundamental oscillations at 534 GHz. A strong DC component and negligible 2nd and 3 rd harmonic oscillations can also be observed in the current spectrum not shown in the figures. A high pass filter can be applied to eliminate the DC component of the output signal. The device has a total radiated power of 0.4 μW at the fundamental frequency. Fig. 3 shows the 3D far-field plot of the oscillator at the fundamental frequency. Note its resemblance to that of a dipole antenna due to similarities in geometry and current distribution.

B. Synchronization in Coupled Devices

It is expected that when two devices are coupled together in an array configuration, as shown in Fig. 4 the total radiated power can be increased by some significant factor. Due to interference and mutual coupling the exact amplification pattern and the effect on the frequency and directivity of the device as a whole is not easily predicted. In order to achieve this however both devices are required to coherently oscillate with the same frequency. Fig. 5 shows the observation of mutual coupling between two RTD oscillators placed side by side each other. The devices have similar dimensions as the single oscillator described in

Section III-A and are separated by a distance $d = 10 \mu$m, with a ground plane of 85 μm $\times$ 55 μm lying 6 μm below the bottom plates of both devices. The space between the oscillators and the ground plane has the same properties as the surrounding medium. As electromagnetically small devices, both oscillators lie within the inductive near field of each other. This is the expected region to achieve coupling, with a stronger transfer of energy the closer the devices lie to each other. Individually, both oscillators operate at distinctly different frequencies, as can be seen in Fig. 5(a) and (b). This is achieved by adjusting the area of the overlapping region between the plates to change the capacitance. Both oscillators are biased at the same voltage but made to have slightly different I-V characteristics as could be expected of any two separate devices for example due to tolerances and uncertainty in manufacturing (see Fig. 5(c)).

During simultaneous operation, it is found that both oscillators lock into a single frequency of 423 GHz, as shown in Fig. 5(d) and (e) with a coupling coefficient of $k \approx 0.28$ (determined from the self and mutual inductances of the device). Figs. 5(f) and 6 shows the far-field radiated away from the device and the distribution of surface currents at the fundamental frequency of the coupled system.

TABLE I

COUPLING FREQUENCIES FOR TWO OSCILLATORS PLACED AT d DISTANCE APART. OSCILLATOR 1 IS FIXED AND THE OVERLAPPING LENGTH OF THE PLATES THAT MAKE UP OSCILLATOR 2 IS SET TO $xgap$ TO ADJUST ITS GEOMETRICAL CAPACITANCE. REGIONS WHERE BOTH OSCILLATORS COUPLE IS HIGHLIGHTED.

| | | | $d=0.004\lambda$ | | $d=0.01\lambda$ | | $d=0.02\lambda$ | | $d=0.03\lambda$ | | $d=0.04\lambda$ | | $d=0.05\lambda$ | |
$xgap$	$f1$	$f2$	$cf1$	$cf2$	$cf1$	$cf2$	$cf1$	$cf2$	$cf1$	$cf2$	$cf1$	$cf2$	$cf1$	$cf2$
3.0	443	495	441	494	441	496	442	496	442	496	442	496	443	496
3.4	443	483	440	483	440	484	441	484	442	484	442	484	442	484
3.8	443	471	439	439	439	473	441	473	441	473	442	473	442	472
4.2	443	461	437	437	438	438	440	440	440	462	442	462	442	461
4.6	443	451	433	433	434	434	436	436	438	438	439	439	441	441
5.0	443	443	429	429	430	430	432	432	433	433	435	435	436	436
5.4	443	437	426	426	427	427	429	429	430	430	432	432	433	433
5.8	443	431	423	423	424	424	426	426	427	427	428	428	444	430
6.2	443	426	420	420	421	421	422	422	445	423	445	425	444	425
6.6	443	422	416	416	417	417	446	418	445	419	445	420	444	420
7.0	443	417	413	413	413	413	446	414	445	415	445	415	444	416
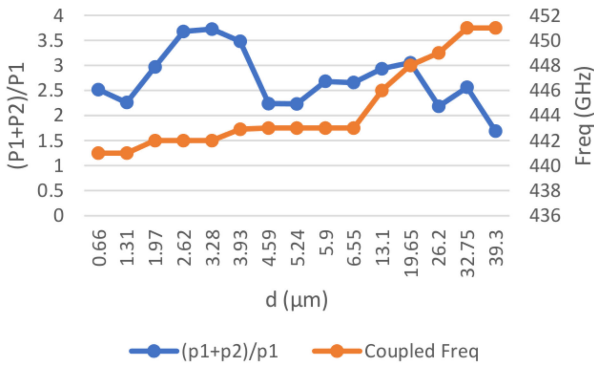
Fig. 7. The relative power of two coupled oscillators and a single oscillator versus separation distance. Orange line (online) shows the coupling frequency.

C. Coherent Power Combination

The total radiating power for oscillators 1 and 2 in the subsection above are calculated to be 0.59 μW and 0.35 μW respectively, while the power of the coupled system is calculated at 1.04 μW in the fundamental mode. It is noted that the combined output power is slightly higher than the sum of the two oscillators. When two oscillators have similar output power and frequencies in a free running condition, their combined power can be nearly 4 times (N^2 where N is the number of oscillators) that of a single oscillator [3], [4]. Fig. 7 shows the relative power of two dissimilar but coupled oscillators and a single oscillator at different separation without a metallic ground plate. It can be seen that it is possible to achieve power amplification of approximately 3.7 times the single oscillator when separated at $d = 3.28\mu$m from each other. If we adjust the fundamental frequency of the second oscillator by adjusting the gap length between the plates that make up the device while keeping that of oscillator 1 at $xgap = 5\mu$m (see Fig. 1), and plot the total power radiated at different distances from the first oscillator as shown in Fig. 8(a), we can deduce that the highest power is achievable when the oscillators are identical and the individual frequencies of both oscillators coincide. This is the case even when the coupling strength is less than that between two non-identical oscillators i.e there isn't a linear correlation between the coupling coefficient and the output power of two coupled devices. Fig. 8(b) and table I shows that there is substantial increase in the output power in the region where the
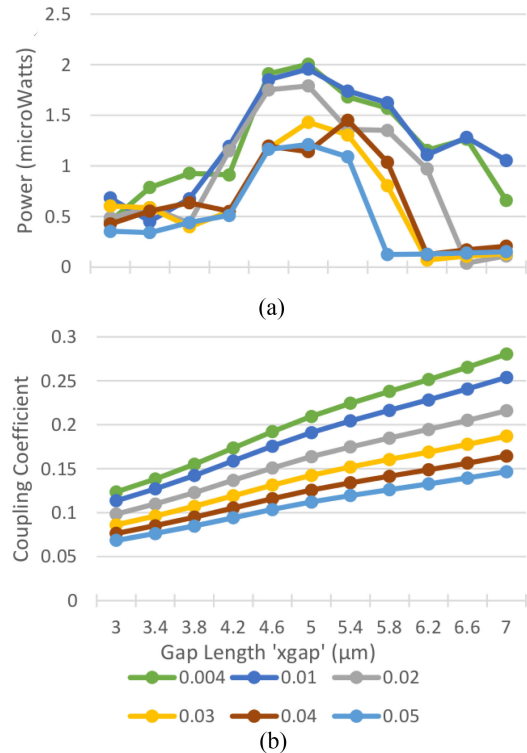

Fig. 8. (a) Total output power of two oscillators placed d distance apart. (b) Coupling coefficient k of two oscillators placed d distance apart. $xgap$ adjusts the length and thus the area of the overlapping region of oscillator 2.

devices couple. Also, increasing the overlapping area between the plates of oscillator 2 allows for greater coupling between the oscillators, and this drops the farther the oscillators are placed from each other. Moreover, sufficient coupling strength is necessary for the the devices to achieve mutual coupling and synchronisation. This is dependent not only on the difference in individual oscillation frequencies but also on the structure of the radiator, phase difference, placement and position, lumped impedances and bias voltage in a non-trivial way.

IV. CONCLUSION

This paper has demonstrated the modeling of a resonant tunneling diode oscillator using a time-domain boundary element method. A reduced method to aid convergence of the non-linear

solver was also presented. Generation of oscillations in the sub-THz range and the synchronisation of 2 oscillators was shown. Comparisons with approximate circuit simulations show reasonable agreement. In simple cases the results match well with those from the full-wave solver. Implications of mutual coupling of the devices on the output power was discussed, with simulations showing a combined power of almost four times a single oscillator. Parameters such as the far-field and face currents not computable using circuit methods are also presented. Future work will focus on the incorporation of the semi-conductors, insulators, and substrates in the model and on the accurate modelling of the effect of their presence on the device characteristics.

ACKNOWLEDGMENT

REFERENCES

[1] D. Saeedkia, *Handbook of Terahertz Technology for Imaging, Sensing and Communications*. Amsterdam, The Netherlands: Elsevier, 2013.

[2] R. Tsu and L. Esaki, "Tunneling in a finite superlattice," *Appl. Phys. Lett.*, vol. 22, no. 11, pp. 562–564, 1973, doi: 10.1063/1.1654509.

[3] M. Asada, S. Suzuki, and N. Kishimoto, "Resonant tunneling diodes for sub-terahertz and terahertz oscillators," *Japanese J. Appl. Phys.*, vol. 47, no. 6R, 2008, Art. no. 4375. [Online]. Available: http://stacks.iop.org/1347-4065/47/i=6R/a=4375

[4] M. B. Gaifullin *et al.*, "Microwave generation in synchronized semiconductor superlattices," *Phys. Rev. Appl.*, vol. 7, Apr. 2017, Art. no. 044024, doi: 10.1103/PhysRevApplied.7.044024.

[5] J.-P. Berenger, "A perfectly matched layer for the absorption of electromagnetic waves," *J. Comput. Phys.*, vol. 114, no. 2, pp. 185–200, 1994. [Online]. Available: http://www.sciencedirect.com/science/article/pii/S0021999184711594

[6] K. Aygun, B. C. Fischer, J. Meng, B. Shanker, and E. Michielssen, "A fast hybrid field-circuit simulator for transient analysis of microwave circuits," *IEEE Trans. Microw. Theory Techn.*, vol. 52, no. 2, pp. 573–583, Feb. 2004.

[7] A. E. Yilmaz, J.-M. Jin, and E. Michielssen, "A parallel FFT accelerated transient field-circuit simulator," *IEEE Trans. Microw. Theory Techn.*, vol. 53, no. 9, pp. 2851–2865, Sep. 2005.

[8] S. O. Lasisi, K. Cools, T. M. Benson, G. Gradoni, and M. T. Greenaway, "An enriched RWG basis for enforcing global current conservation in em modelling of capacitance extraction," in *Proc. Int. Conf. Electromagnetics Adv. Appl.*, 2017, pp. 1369–1372.

[9] J. Gaskell *et al.*, "Graphene-hexagonal boron nitride resonant tunneling diodes as high-frequency oscillators," *Appl. Phys. Lett.*, vol. 107, no. 10, 2015, Art. no. 103105, doi: 10.1063/1.4930230.

[10] A. Mishchenko *et al.*, "Twist-controlled resonant tunnelling in graphene/boron nitride/graphene heterostructures," *Nature Nanotechnol.*, vol. 9, no. 10, pp. 808–813, Oct. 2014, doi: 10.1038/nnano.2014.187.

[11] L. Esaki, "New phenomenon in narrow germanium $p - n$ junctions," *Phys. Rev.*, vol. 109, pp. 603–604, Jan. 1958, doi: 10.1103/PhysRev.109.603.

[12] N. Holonyak, I. A. Lesk, R. N. Hall, J. J. Tiemann, and H. Ehrenreich, "Direct observation of phonons during tunneling in narrow junction diodes," *Phys. Rev. Lett.*, vol. 3, pp. 167–168, Aug. 1959, doi: 10.1103/PhysRevLett.3.167.

[13] M. E. Hines, "High-frequency negative-resistance circuit principles for esaki diode applications," *Bell Syst. Tech. J.*, vol. 39, no. 3, pp. 477–513, May 1960.

[14] C. Liu, J. W. Massey, and A. E. Yılmaz, "A nonradiating finite-gap lumped-port model," *IEEE Antennas Wireless Propag. Lett.*, vol. 17, no. 7, pp. 1339–1343, Jul. 2018.

[15] C. Liu and A. E. Yilmaz, "A generalized finite-gap lumped-port model," in *Proc. IEEE 27th Conf. Elect. Perform. Electron. Packag. Syst.*, 2018, pp. 173–175.